Analytica Chimica Acta 1420 (2026) 345971

Contents lists available at ScienceDirect

Analytica Chimica Acta

journal homepage: www.elsevier.com/locate/aca

Designing versatile sandwich-like magnetic Nb_2O_5 nanocomposites derived from Nb_2C MXene for phosphopeptide enrichment

Sen Zhang, Yan Lu, Jun-qin Qiao, Hong-zhen Lian *

State Key Laboratory of Analytical Chemistry for Life Science, School of Chemistry & Chemical Engineering and Center of Materials Analysis, Nanjing University, 163 Xianlin Avenue, Nanjing, 210023, China

HIGHLIGHTS

- Fe_3O_4 was in situ grown on Nb_2CT_x MXene layers to form a sandwich-like structure.
- Nb_2C–Fe_3O_4 composites were calcined in air to allow the transformation to oxides.
- The magnetic m-Nb_2O_5–Fe_2O_3 can enrich phosphopeptides through MOAC by Nb and Fe.
- The sandwich-like composites showed satisfactory performance in multiple aspects.
- Non-fat milk, human saliva and TCMI confirmed the applicability of the composites.

GRAPHICAL ABSTRACT

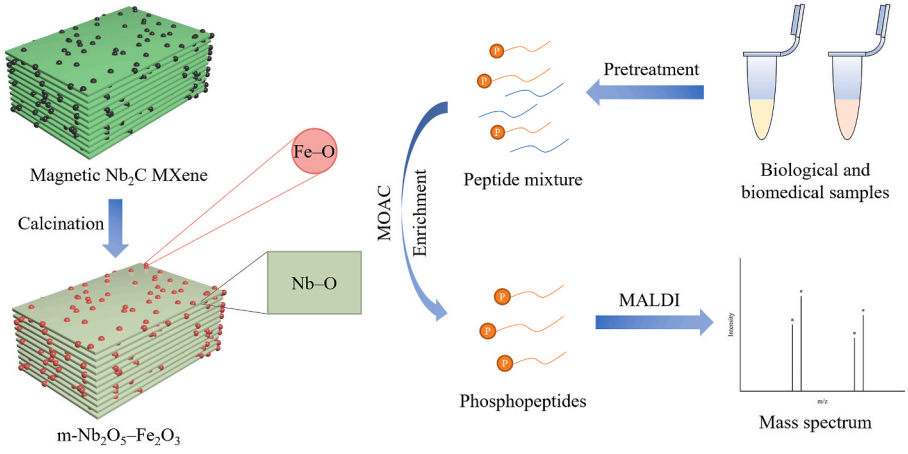

ARTICLE INFO

Handling Editor: Xiu-Ping Yan

Keywords:
Nb_2CT_x MXene
Magnetic solid-phase extraction (MSPE)
Metal oxide affinity chromatography (MOAC)
Phosphopeptides enrichment
Traditional Chinese medicine injections (TCMIs)

ABSTRACT

Background: The enrichment of phosphopeptides prior to their detection is essential for the identification of protein phosphorylation followed by matrix assisted laser desorption/ionization time-of-flight mass spectrometry because of their low concentration, low deionization efficiency and suppression from the interference derived from high-abundance counterparts. Niobium-based affinity materials have great potential in the enrichment of phosphopeptide enrichment, yet have not been extensively studied. To date, there are no reports on the application of Nb_2CT_x-based materials in separation science, especially in the application in phosphopeptide enrichment.

Results: In this work, Nb_2C MXene derived sandwich-like magnetic Nb_2O_5 nanocomposites (denoted as m-Nb_2O_5–Fe_2O_3) were designed and synthesized for the first time by HF-etching of Nb_2AlC MAX phase, in situ growth of Fe_3O_4 nanoparticles and calcination in air. The nanocomposites were then applied as magnetic solid-phase extraction (MSPE) adsorbents in the enrichment of phosphopeptides through the synergistic metal oxide affinity chromatography mechanism by Nb–O and Fe–O. The MSPE method exhibited extremely low detection limit (0.1 nmol L^{-1} of β-casein), great anti-interference ability (1:2000 of the molar ratio of β-casein to bovine

* Corresponding author.
E-mail address: hzlian@nju.edu.cn (H.-z. Lian).

https://doi.org/10.1016/j.aca.2026.345971
Received 30 May 2026; Received in revised form 9 July 2026; Accepted 12 July 2026
Available online 13 July 2026

serum albumin), good reusability (3 cycles) and satisfactory recovery (87.6%). The universality of m-Nb_2O_5–Fe_2O_3 was further verified by the successful application in non-fat milk, human saliva and a traditional Chinese medicine injection.

Significance: The m-Nb_2O_5–Fe_2O_3 nanocomposites are able to enrich phosphopeptides with high efficiency from diverse samples, thanks to the layered structure which provides abundant specific binding sites of Nb–O and Fe–O towards phosphate groups in phosphopeptides. The composites show great potential as a promising material for phosphopeptide enrichment from complex biological and biomedical samples.

1. Introduction

As one of the most important post-translational modifications of proteins, phosphorylation plays significant roles in multiple biological processes including cell growth, cell differentiation, signal transduction and so on [1,2]. Abnormal protein phosphorylation is related to diseases such as cancer [3], Alzheimer's disease [4], Parkinson's disease [5], etc. Currently, bottom-up strategy is one of the primary techniques to analyze the protein phosphorylation with the assistance of mass spectrometry (MS). On the other hand, matrix assisted laser desorption/ionization time-of-flight mass spectrometry (MALDI-TOF MS) has been widely used to identify phosphorylated peptides/proteins thanks to its excellent sensitivity, high throughput, fast analysis speed and wide dynamic range [6,7]. However, owing to the low concentration, low deionization efficiency and suppression from the interference derived from high-abundance counterparts, it has received great attention to the development of approaches to efficiently enrich phosphopeptides from the complex matrices prior to the detection by MALDI-TOF MS [8,9].

To date, there are multiple strategies employed for enrichment of phosphopeptides/phosphoproteins such as ion-exchange chromatography [10,11], immunoprecipitation [12], immobilized metal ion affinity chromatography (IMAC) [13], metal oxide affinity chromatography (MOAC) [14], etc. Among them, IMAC and MOAC have attracted lots of attention due to the special affinity of metal ions/metal oxides with phosphate groups in phosphopeptides/phosphoproteins.

The metals employed for IMAC and MOAC are typically high-valence transition metals (III and higher), as these metals possess sufficient orbitals to enable the coordination with oxygen atoms in phosphate groups. Among them, titanium [15,16], zirconium [17,18], and iron [19,20] have been widely exploited to prepare IMAC or MOAC materials for phosphopeptide enrichment. Niobium, adjacent to zirconium in the periodic table and possessing a common state of high-valence state (V), is a promising metal candidate for IMAC and MOAC materials which has strong affinity for phosphopeptides/phosphoproteins. Nevertheless, there are only one or two reports on niobium-based MOAC materials for phosphopeptide enrichment. Ficarro et al. [21] pioneered the application of niobium oxide in phosphoproteomics and found that Nb_2O_5 provided effective enrichment and recovery of phosphopeptides. Lin et al. [22] then synthesized a core-shell niobium oxide-coated magnetic nanoparticles Fe_3O_4@Nb_2O_5 by introducing Fe_3O_4 as the magnetic core for magnetic solid-phase extraction (MSPE) of phosphopeptides, which simplified the operation procedure. Meanwhile, a few magnetic Nb (V)-based IMAC materials were also prepared. Li and Li's group [23,24] utilized the phenolic hydroxyl groups on polydopamine to immobilize Nb^{5+} ions. The resulting Fe_3O_4@PDA–Nb^{5+} exhibited satisfactory performance in the enrichment for phosphopeptides. They [25] further incorporated Ti(IV) into the system, and Fe_3O_4@PDA–Ti/Nb showed increased enrichment performance for phosphopeptides in comparison with that of Ti(IV) or Nb(V) alone. Yan and Ding's group involved a chelating ligand aminomethylphosphonic acid on magnetic core-shell nanoparticles (Fe_3O_4@$mSiO_2$@APA@ Ti^{4+}/Nb^{5+}) [26] and another chelating ligand thioglycolic acid on covalent organic framework (COF–S–S–COOH–Ti^{4+}/Nb^{5+}) [27] to enhance the performance of Ti/Nb bimetallic IMAC materials. However, to our knowledge, no other attractive forms of Nb-based advanced functional materials have been explored for the enrichment for phosphopeptides.

MXenes, produced by etching out A layers from MAX phase, are a large family of two-dimensional (2D) metal carbides or nitrides, usually denoted as $M_{n+1}X_nT_x$ based on its composition, where M stands for one or more early transition metals, A is mainly a group IIIA or IVA element, X is C and/or N, T represents terminal groups (–O, –F and/or –OH) and $n = 1$, 2 or 3 [28]. As a kind of MXene, Nb_2CT_x is drawing more and more attention by researchers and has been studied in energy storage [29], electrochemical sensing [30], photocatalysis [31], electrochemiluminescence [32], etc. The family member of MXenes $Ti_3C_2T_x$ and $Ti_3C_2T_x$-based materials have been extensively studied for the enrichment of phosphopeptides. These materials include Ti_3AlC_2 MAX phase and bare $Ti_3C_2T_x$ [33], Fe_3O_4/TiO_2@$Ti_3C_2T_x$ with MXene-generated TiO_2 on the surface [34], polyamidoamine dendrimer (PAMAM) modified magnetic Ti_3C_2 MXene [35], $Ti_3C_2T_x$/UiO-66–NH_2 composites prepared by dielectric barrier discharge [36], metal-phenolic network-modified magnetic Ti_3C_2 MXene [37], polycrystalline TiO_2 generated on Ti_3C_2 MXene [38], dTi-MMX with TiO_2 coated on magnetic Ti_3C_2 MXene [39]. In our previous work [40], exfoliated Ti_3C_2 MXene was decorated with Fe_3O_4 nanoparticles to form Ti_3C_2–Fe_3O_4 nanosheets for satisfactory phosphopeptide enrichment. Another work by our group [41] grew UiO-66–NH_2 nanocrystals on Ti_3C_2 nanosheets and derived the composites to oxides, forming a potato-chip-like structure. Magnetite nanoparticles were further in situ generated on the potato-chip-like nanosheets to endow the material with magnetism. The resulted trimetallic oxides were utilized to more effectively enrich phosphopeptides. However, to date, there are no reports on the application of Nb_2CT_x-based materials in separation science, especially not to mention the application in phosphopeptide enrichment. Moreover, there have been scarce researches on magnetic Nb_2C MXene-based nanocomposites. To the best of our knowledge, only Zhao's group [30] reported Nb_2C/$MnFe_2O_4$ for the electrochemical sensing of acetaminophen and dopamine.

Herein, we designed and synthesized a sandwich-like magnetic Nb_2C MXene-derived nanocomposite m-Nb_2O_5–Fe_2O_3 for phosphopeptide enrichment. Nb_2C MXene was obtained by etching Nb_2AlC using HF and then Fe_3O_4 nanoparticles were in situ grown on it. Afterwards, by calcination in air, niobium oxide was generated in situ on the surface of Nb_2C MXene. Meanwhile, magnetite nanoparticles were transformed into maghemite. The sandwich-like structure provides abundant binding sites. With the synergistic MOAC mechanism by Nb_2O_5 and γ-Fe_2O_3, the magnetic nanocomposites m-Nb_2O_5–Fe_2O_3 exhibit efficient and selective enrichment performance for phosphopeptides by MSPE. Real-world complex biological and biomedical samples including non-fat milk, human saliva and traditional Chinese medicine injections (TCMIs) were explored to investigate the reliability and applicability of m-Nb_2O_5–Fe_2O_3.

2. Experimental section

2.1. Synthesis of m-Nb_2O_5–Fe_2O_3

The whole synthesis process of m-Nb_2O_5–Fe_2O_3 is illustrated in Scheme 1A. Firstly, Nb_2CT_x MXene was obtained by etching Nb_2AlC MAX phase. In detail, 1.0 g of Nb_2AlC was slowly added into 20 mL of 50% HF under stirring at 50 °C. After the mixture was stirred for 48 h, it was centrifugated at 5000 rpm for 1 min. Then the sediment was washed

with water several times until the pH of the supernatant was >6. The obtained Nb_2CT_x MXene was dried under vacuum at 60 °C. Subsequently, Nb_2CT_x MXene was endowed with magnetism by the in situ growth of Fe_3O_4 nanoparticles. That is, 100 mg Nb_2CT_x was dispersed into 80 mL water and sonicated for 30 min. Another 20 mL water containing 180 mg $FeSO_4$•$7H_2O$ was added into the dispersion. The sonication continued for another 1 h. Then 10 mL ammonia (25%) was added and the mixture was stirred being exposed in air for 1 h. The product was collected with the assistance of a magnet, washed with water and dried in vacuum at 60 °C. Finally, Nb_2C–Fe_3O_4 was calcined in air at 500 °C for 5 h with a heating rate of 5 °C•min^{-1} to allow the formation of Nb_2O_5 on the MXene, obtaining m-Nb_2O_5–Fe_2O_3.

Details regarding all chemicals and reagents and characterization of the materials are provided in the Supplementary material.

2.2. Sample preparation

The samples were prepared for phosphopeptides enrichment based on our previous work [40]. Detailed procedures are described in the Supplementary material.

2.3. Enrichment of phosphopeptides

The workflow of enriching phosphopeptides is shown in Scheme 1B. In advance of the enrichment, *β*-casein digests were diluted with loading solution (50% ACN - 2% TFA) to 10^{-1} μmol L^{-1}, non-fat milk digests were diluted 500 times, human saliva was diluted 20 times, and the RDNI remnants were re-dissolved in 1.0 mL loading buffer. After 10 μL of m-Nb_2O_5–Fe_2O_3 dispersion of 20 mg mL^{-1} was added to 100 μL of the sample solution, the mixture was vortexed at room temperature for 25 min. The resulting sediment was separated with the assistance of a magnet. After being washed with loading buffer for 3 times, 5.0 μL of 10% NH_3•H_2O was added to elute the adsorbed phosphopeptides in a sonication bath for 10 min. The eluate was then detected by MALDI-TOF MS about which the details are supplied in the Supplementary material.

2.4. Enrichment recovery of phosphopeptides

Two aliquots of standard phosphopeptides LRRA[pS]LGGK were differentially labelled with CH_2O (light isotope) or CD_2O (heavy isotope), causing a mass increase of 56 or 64 Da. Then, heavy isotope-labelled phosphopeptides were subsequently enriched by m-Nb_2O_5–Fe_2O_3, and the eluate was mixed with an equal amount of light-isotope-labelled phosphopeptides, followed by MALDI-TOF MS analysis. The ratio of peak area of two labelled phosphopeptides was calculated to determine the recovery. In parallel, equal amounts of the two isotopically labelled phosphopeptides without enrichment were mixed and analyzed as control to eliminate the effects of labelling efficiency.

3. Results and discussion

3.1. Synthesis and characterization of m-Nb_2O_5–Fe_2O_3

The morphology of Nb_2AlC, Nb_2CT_x, Nb_2C–Fe_3O_4 and m-Nb_2O_5–Fe_2O_3 was characterized by SEM and TEM as shown in Fig. 1. According to Fig. 1A and E, Nb_2AlC MAX phase exhibits a bulk structure before etching. After Al layer in Nb_2AlC was etched out by HF, Nb_2CT_x shows an accordion-like structure (Fig. 1B and F). Then with the in situ growth of Fe_3O_4 nanoparticles, nanospheres could be seen on the surfaces and between the layers of Nb_2CT_x MXene, forming a sandwich-like structure of Nb_2C–Fe_3O_4 (Fig. 1C and G). After being finally calcined in air, the sandwich-like morphology maintained or not significantly changed (Fig. 1D and H). EDS results of the four materials are shown in Fig. S1–S4 and Table S1, based on which, it can be inferred that C and Nb were uniformly distributed on all the materials. After etching, Al contents (weight percentage) in the material sharply decreased from 6.8% to 0.6%. Besides, oxygen and fluorine could be detected with weight percentages of 16.3% and 5.4% respectively, indicating the removal of Al layer and the appearance of terminal groups (–O, –F and –OH). Then, due to the alkaline condition during the growth of Fe_3O_4 nanoparticles, the remaining Al dissolved and fluorine atoms on the MXene surface were replaced by hydroxyl groups, causing F and Al were no longer detected by EDS. Furthermore, after calcination in air, an increase in the weight percentage of oxygen was observed from 9.0% to 27.1%, suggesting the oxidation of Nb_2C and Fe_3O_4 in the nanocomposites.

FT-IR and Raman spectra were further used to characterize the functional groups in the materials. As shown in Fig. 2A, the peaks at 616 and 645 cm^{-1} were attributed to the in-plane vibration and out-of-plane vibration along *c*-axis of C atoms, and the peak at 462 cm^{-1} was assigned to the out-of-plane vibration along *c*-axis of Al atoms in Nb_2AlC [42]. After being etched, the two peaks associated with C atoms shifted to 673 and 555 cm^{-1} due to the influence of the terminal groups. Besides, the peak associated with Al atoms at 462 cm^{-1} disappeared, suggesting the removal of Al layer. At the same time, a new peak at 889 cm^{-1} appeared, which was assigned to the stretching vibration of Nb–O bonds on the surface [43]. The spectrum of Nb_2C–Fe_3O_4 shows peaks at 576, 886 and 1404 cm^{-1}, ascribed to the stretching vibration of Fe–O bonds, the stretching vibration of Nb–O bonds and the bending vibration of O–H bonds, respectively. After calcination, the peak of Nb–O bonds slightly shifted to 897 cm^{-1}, and that of Fe–O bonds split into two peaks at 643 and 582 cm^{-1}, which is a sign of the formation of γ-Fe_2O_3 [44]. Raman spectra of the materials are depicted in Fig. 2B. Before etching, the peak at 133 cm^{-1} in the spectrum of Nb_2AlC corresponds to the in-plane oscillations of Nb and C atoms (ω_1, E_{2g} symmetry). The peak at 187 cm^{-1} is attributed to the in-plane oscillation of Al atoms (ω_3, E_{2g} symmetry). The peak at 265 cm^{-1} originates from the out-of-plane vibrations of Nb and C atoms (ω_4, A_{1g} symmetry). The peak at 651 cm^{-1} is assigned to the

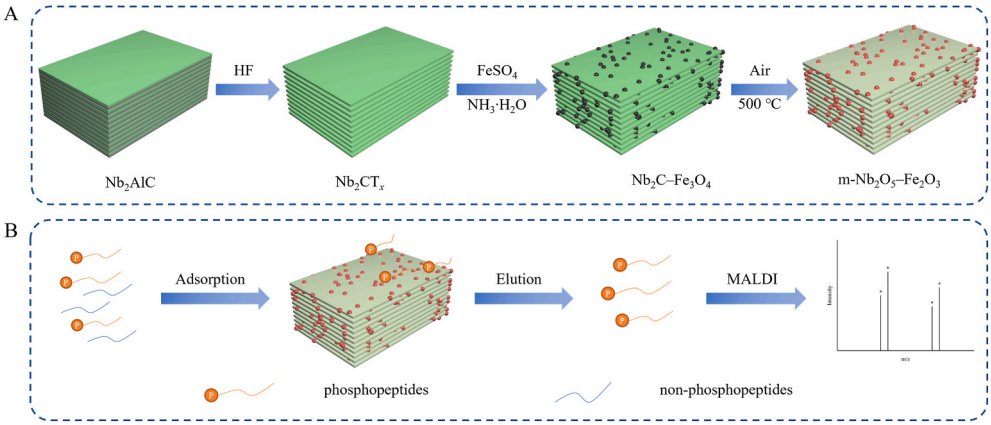

Scheme 1. Schematic diagram of the synthesis of m-Nb_2O_5–Fe_2O_3 (A) and the procedure of enriching phosphopeptides (B).

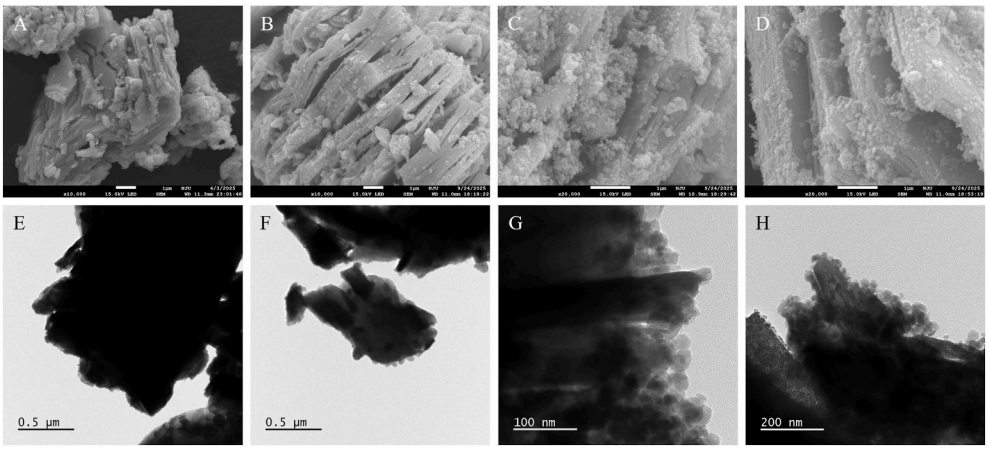

Fig. 1. SEM (A–D) and TEM (E–H) images of Nb_2AlC (A, E), Nb_2CT_x (B, F), Nb_2C–Fe_3O_4 (C, E) and m-Nb_2O_5–Fe_2O_3 (D, H).

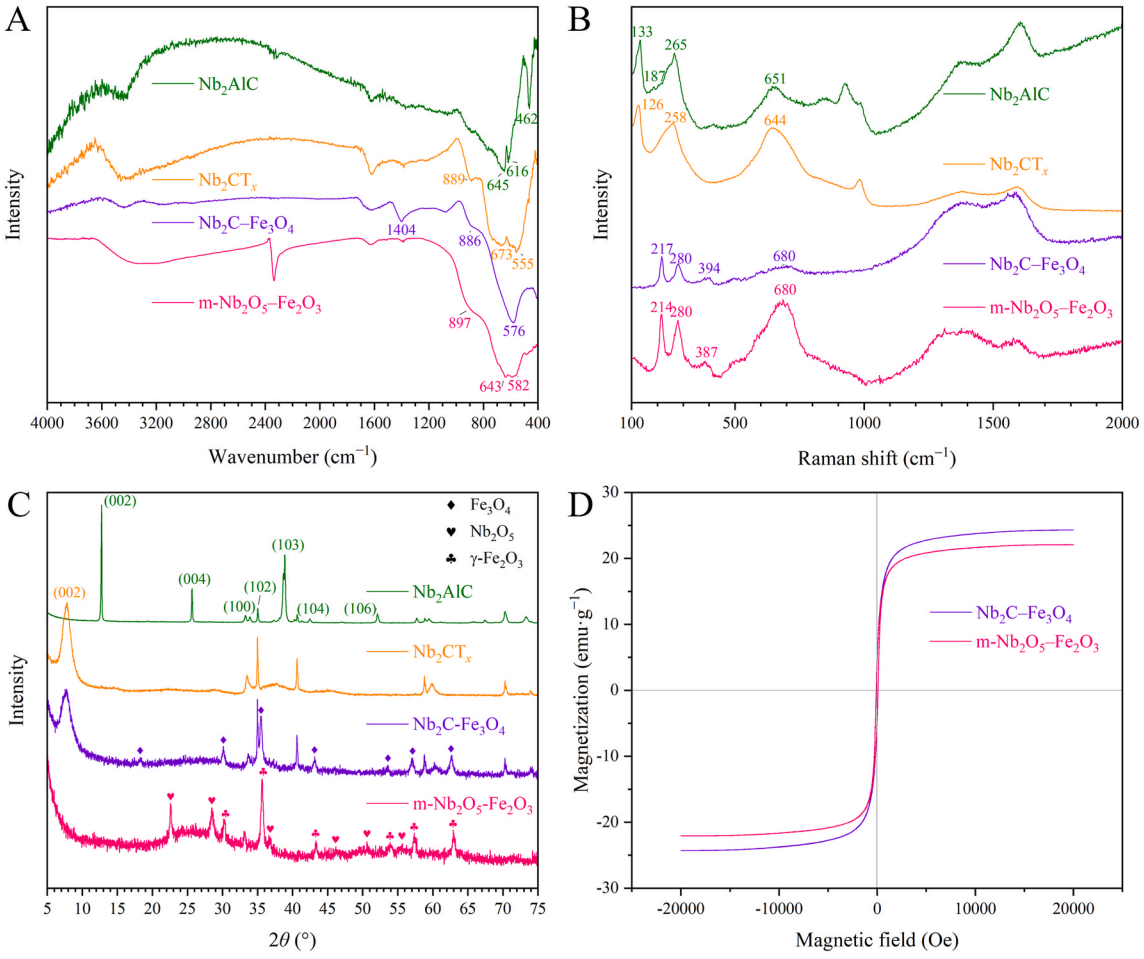

Fig. 2. FT-IR spectra (A), Raman spectra (B) and XRD patterns (C) of Nb_2AlC, Nb_2CT_x, Nb_2C–Fe_3O_4 and m-Nb_2O_5–Fe_2O_3, and hysteresis loops (D) of Nb_2C–Fe_3O_4 and m-Nb_2O_5–Fe_2O_3.

stretching vibration of Nb–C bonds (A_{1g} symmetry). After being etched, the peaks around 133, 265 and 651 cm^{-1} almost remained, because these vibration modes consist of no vibration of Al atoms. Meanwhile, the peak at 187 cm^{-1} disappeared, confirming the successful removal of Al layer [45]. After in situ growth of Fe_3O_4 nanoparticles onto Nb_2CT_x MXene, the Raman spectrum is dominated by characteristic peaks of Fe_3O_4 located at 217, 280, 394 and 680 cm^{-1}, corresponding to the T_{2g}, E_g, T_{2g} and A_{1g} vibration modes of Fe–O bonds [46]. The intrinsic peaks assigned to Nb_2C MXene is significantly suppressed for the reason that the surface of Nb_2C MXene is covered by Fe_3O_4 nanoparticles and thus cannot be recognized. After calcination, the spectrum of m-Nb_2O_5–Fe_2O_3 exhibits peaks at 214, 280, 387 and 680 cm^{-1}, very close to those in the spectrum of Nb_2C–Fe_3O_4, due to the similarity of the spectra between Fe_3O_4 and γ-Fe_2O_3 and possible transformation to α-Fe_2O_3 under the laser [47].

XRD was used to characterize the crystal structure of Nb_2AlC,

Nb_2CT_x, Nb_2C–Fe_3O_4 and m-Nb_2O_5–Fe_2O_3. As shown in Fig. 2C, the XRD pattern of Nb_2AlC displays characteristic peaks of Nb_2AlC MAX phase (PDF #00-030-0033) located at 12.7°, 25.7°, 33.3°, 35.0°, 38.9°, 42.5° and 52.1°, corresponding to the (002), (004), (100), (102), (103), (104) and (106) planes. After being etched, the diffraction peaks associated to the non-basal planes vanished including (103), (104) and (106), remaining peaks of (002) and (100) planes. Coincidently, due to the existence of small amount of Nb_4C_3 (PDF #97-004-2758) in the raw MAX material the diffraction peaks of which were hidden in Nb_2AlC, the peaks at 35.0°, 40.6° and 58.8° in the diffraction pattern are not ascribed to the structure of Nb_2CT_x, but the impurity in the raw material. The pattern of Nb_2C–Fe_3O_4 not only exhibits peaks of (002) and (100) planes of Nb_2CT_x, but also the characteristic peaks of magnetite (PDF #97-002-6410). Finally, with the oxidation in air, Nb_2O_5 and γ-Fe_2O_3 formed. Thus, the XRD pattern of m-Nb_2O_5–Fe_2O_3 includes peaks of niobium oxide (PDF #97-000-1840) and maghemite (PDF #97-008-7121).

To examine the magnetic property of Nb_2C–Fe_3O_4 and m-Nb_2O_5–Fe_2O_3, their hysteresis loops were measured and depicted in Fig. 2D. It can be seen that both magnetic materials are superparamagnetic and the saturation magnetization of Nb_2C–Fe_3O_4 and m-Nb_2O_5–Fe_2O_3 are 24.3 and 22.0 emu•g^{-1}, respectively, satisfying the demand of MSPE.

In order to investigate the processes occurring during the calcination, TGA-FT-IR and XPS were carried out. TG curves in air of Nb_2CT_x and Nb_2C–Fe_3O_4 exhibit similar trends (Fig. S5) with three main weight-changing stages, including two weight-loss stages (Stage I: room temperature to ~300 °C; Stage III: ~540 °C to ~680 °C) and one weight-gain stage (Stage II: ~340 °C to ~500 °C). Below ~300 °C, the weight loss was mainly caused by the removal of adsorbed water and ammonia. Then with the temperature increasing, a weight gain was observed which was associated with the oxidation of Nb_2C and the formation of Nb_2O_5. Further heating above ~540 °C caused another weight loss, attributed to the oxidation of carbon, verified by the transmittance-temperature curve at 2304 cm^{-1} which is the characteristic absorption wavenumber of CO_2. Comparing these two TG curves, the relative weight change of Nb_2C–Fe_3O_4 was smaller than that of Nb_2CT_x. This is because Nb_2C constitutes only a part of the composites, whereas Fe_3O_4 undergoes a weight gain when being oxidized at elevated temperature, which partially compensates the weight loss of Nb_2C.

XPS spectra of Nb_2C–Fe_3O_4 and m-Nb_2O_5–Fe_2O_3 are illustrated in Fig. S6. The XPS survey spectra of both materials show peaks of Fe 2p, O 1s, C 1s and Nb 3d, revealing the elemental composition of the two materials. High-resolution XPS spectra of Nb 3d, Fe 2p, O 1s and C 1s are displayed in Fig. 3 and the peak deconvolution results are listed in Table S2. Nb $3d_{5/2}$ and $3d_{3/2}$ peaks of Nb_2C–Fe_3O_4 were deconvoluted into three peaks each, centered at 206.9, 206.5 and 203.8 eV for Nb $3d_{5/2}$ and 209.7, 209.2 and 207.1eV for Nb $3d_{3/2}$, assigned to the niobium in Nb_2O_5, NbO_x and Nb–C, respectively [48]. The Nb 3d spectrum of m-Nb_2O_5–Fe_2O_3 was also deconvoluted into six peaks corresponding to Nb_2O_5 (207.1 and 209.8 eV), NbO_x (206.6 and 209.3 eV) and Nb–C (204.2 and 206.9 eV). Notably, the peaks of Nb–C in m-Nb_2O_5–Fe_2O_3 are quite low and barely identifiable, because the calcination broke the Nb–C bonds and then formed oxides. The Fe 2p spectrum of Nb_2C–Fe_3O_4 was deconvoluted into peaks assigned to Fe(III) $2p_{1/2}$ (724.9 eV), Fe(III) $2p_{3/2}$ (711.5 eV), Fe(II) $2p_{1/2}$ (722.6 eV), Fe(II) $2p_{3/2}$ (709.5 eV) and two satellite peaks (732.1 and 718.7 eV), confirming the presence of Fe_3O_4. Meanwhile, Fe 2p spectrum of m-Nb_2O_5–Fe_2O_3 was deconvoluted into peaks attributed to Fe(III) $2p_{1/2}$ (724.7 eV), Fe(III) $2p_{3/2}$ (711.0 eV) and two satellite peaks (732.6 and 719.0 eV). Peaks of lower binding energies are also observed in the spectrum at 723.1 and 709.8 eV, which

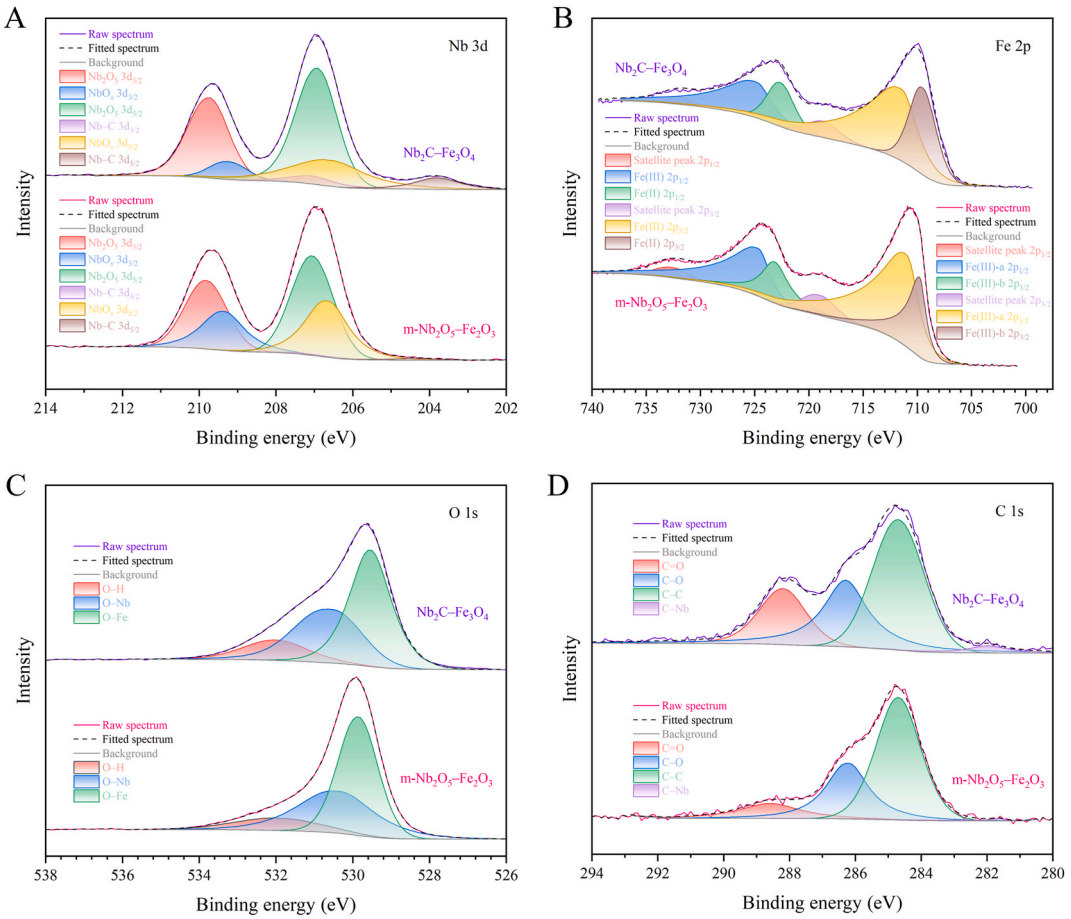

Fig. 3. High-resolution XPS spectra of Nb_2C–Fe_3O_4 and m-Nb_2O_5–Fe_2O_3: Nb 3d (A), Fe 2p (B), O 1s (C) and C 1s (D).

are associated with the surface defects or oxygen vacancies in γ-Fe_2O_3 [49]. The O 1s spectra of Nb_2C–Fe_3O_4 and m-Nb_2O_5–Fe_2O_3 were deconvoluted into 3 peaks assigned to surface O–H, O–Nb and O–Fe, supporting the successful construction of Nb_2C–Fe_3O_4 and m-Nb_2O_5–Fe_2O_3 composites. And the C 1s spectra were deconvoluted into four peaks ascribed to C═O, C–O, C–C and C–Nb. It is worth noting that the normalized peak area of C–Nb decreased after calcination because of the breaking of C–Nb bonds.

BET surface area analysis was performed to investigate the potential adsorption performance of m-Nb_2O_5–Fe_2O_3. The N_2 adsorption/desorption isotherm is drawn in Fig. S7. The BET surface area of m-Nb_2O_5–Fe_2O_3 was calculated to be 27.4 m^2 g^{-1}, on the same scale level with other reported 2D MXene-based materials [50,51].

3.2. Enrichment performance of m-Nb_2O_5–Fe_2O_3 for phosphopeptides

The acidity of the loading buffer plays a crucial role in phosphopeptide enrichment. Therefore, buffers containing 50% ACN and different volume ratios of TFA were used to optimize the loading conditions to enrich phosphopeptides from tryptic digests of β-casein. As shown in Fig. 4, when a low TFA concentration (0% and 0.01%) was used, non-phosphopeptides were identified together with phosphopeptides in the MS spectra after enrichment. As the acidity increased (0.05% and 0.1% TFA), both the number and intensity of non-phosphopeptide peaks decreased markedly while the intensity of identified phosphopeptides increased. When TFA concentration reached 0.5% or higher, the spectrum was dominated by the peaks of phosphopeptides. TFA concentrations of 2.0% and 5.0% resulted in the optimal enrichment performance with the largest number of phosphopeptide peaks. Considering higher acidity causes potential dissolution of the metal oxides, 2.0% was chosen as the optimal concentration of TFA. The information of the phosphopeptides enriched by m-Nb_2O_5–Fe_2O_3 is summarized in Table S3.

To evaluate the anti-interference ability of m-Nb_2O_5–Fe_2O_3, digest mixtures of β-casein and BSA at different molar ratios (1:100, 1:200, 1:500, 1:1000 and 1:2000) was used for phosphopeptide enrichment. As shown in Fig. 5A and B, without enrichment, no phosphopeptides in the mixtures of the five molar ratios were identified caused by the suppression of the non-phosphopeptides of high abundance derived from BSA. After enrichment by m-Nb_2O_5–Fe_2O_3, three phosphopeptides (*m/z* 2061, 2556 and 3122) derived from β-casein were identified in the five MS spectra. It can be seen that with a larger ratio of BSA, a larger amount of non-phosphopeptides were also enriched due to their abundance, and the relative intensity of the interference peaks was higher. However, the number and intensity of phosphopeptide signals was little affected, indicating the powerful anti-interference ability.

The detection limit of the enrichment method was determined by applying m-Nb_2O_5–Fe_2O_3 in different concentrations (5.0, 2.0, 1.0, 0.5, 0.2 and 0.1 nmol L^{-1}) of β-casein digests. As shown in Fig. 5C and D, without enrichment, no peaks of phosphopeptides were detected. After enrichment by m-Nb_2O_5–Fe_2O_3, the peaks of three phosphopeptides derived from β-casein were identified in all six MS spectra, displaying a decreasing trend of the peak intensities with the decrease of the concentration of β-casein digests. Notably, even when the concentration was as low as 0.1 nmol L^{-1}, the signal to noise ratios (S/N) of the peaks at *m/z* 2062, 2556 and 3122 were 6, 7 and 6, respectively (Fig. S8). These results demonstrate the excellent sensitivity to phosphopeptides of the Nb_2O_5–Fe_2O_3-based MSPE method.

The repeatability and the stability of m-Nb_2O_5–Fe_2O_3 in the enrichment of phosphopeptides were examined. The nanocomposites were recycled by washing with 10% NH_3•H_2O for three times and equilibrating with loading buffer before reuse. As shown in Fig. S9, the enrichment performance of m-Nb_2O_5–Fe_2O_3 toward phosphopeptides remained essentially unchanged after the composites being recycled. After three reuse cycles, no significant decrease in the number or the intensity of phosphopeptides enriched was observed, indicating the

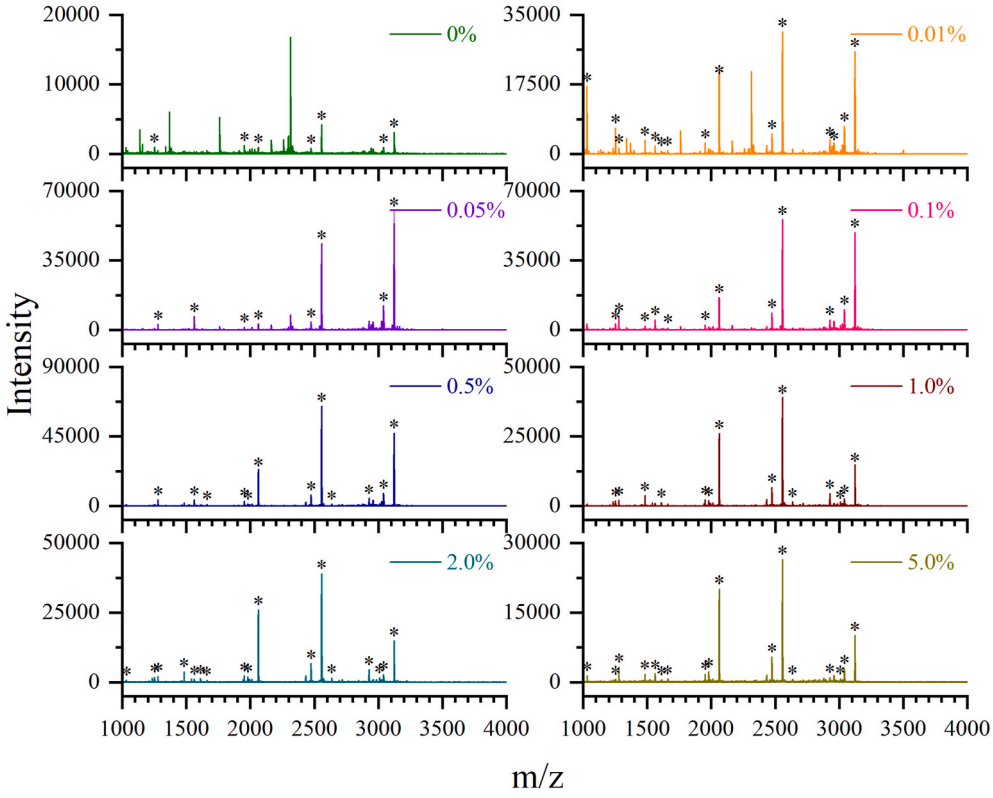

Fig. 4. MALDI-TOF MS spectra of β-casein digests after enrichment with m-Nb_2O_5–Fe_2O_3 using water solutions containing 50% ACN and different percentages of TFA as loading buffer.

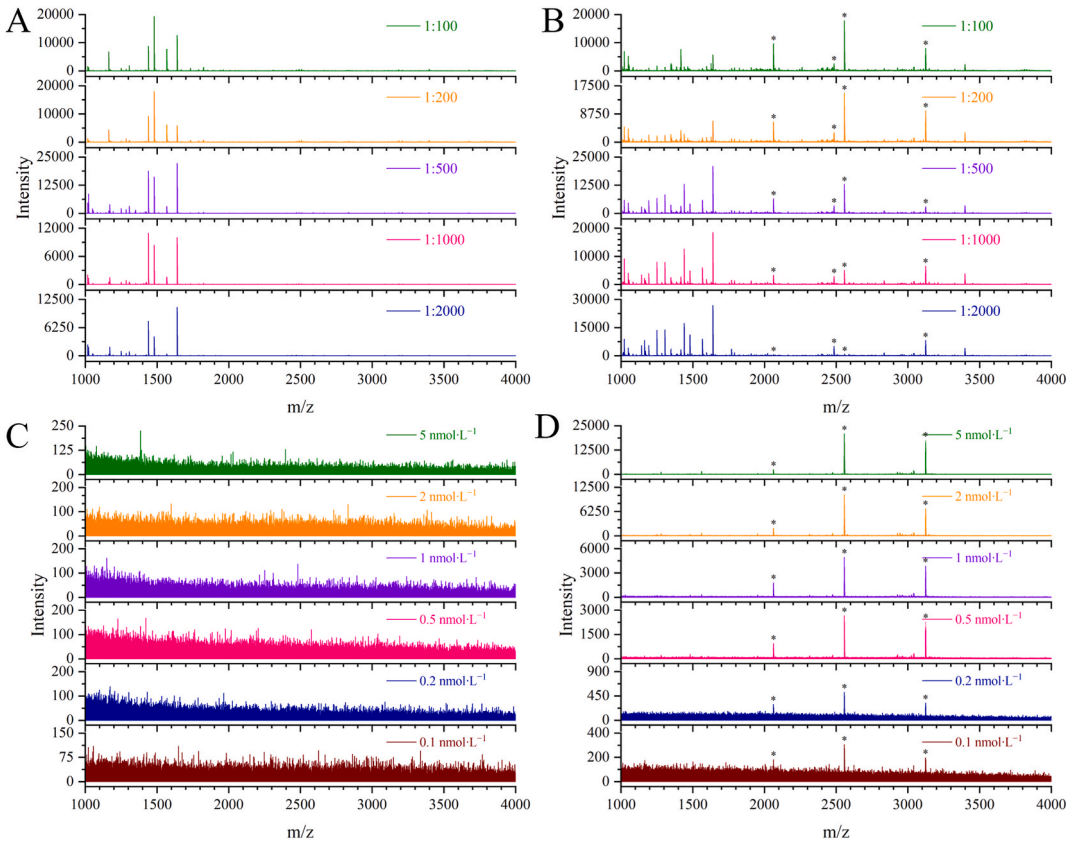

Fig. 5. MALDI-TOF MS spectra of β-casein and BSA digest mixture at different molar ratios before (A) and after (B) enrichment with m-Nb_2O_5–Fe_2O_3, and MALDI-TOF MS spectra of β-casein digests of different concentrations before (C) and after (D) enrichment with m-Nb_2O_5–Fe_2O_3.

satisfactory reusability of m-Nb_2O_5–Fe_2O_3.

To assess the enrichment recovery of m-Nb_2O_5–Fe_2O_3, a standard phosphopeptide LRRA[pS]LGGK was isotopically labelled and utilized as a model sample. As shown in Fig. S10 and Table S4, the calculated recovery was 87.6%, which testifies the competence of m-Nb_2O_5–Fe_2O_3 as an excellent MSPE adsorbent for phosphopeptides.

3.3. Application in real samples

Non-fat milk was preliminarily used to examine the applicability of m-Nb_2O_5–Fe_2O_3 in complex samples. As shown in Fig. S11, without enrichment, the MS spectrum was dominated by non-phosphopeptide peaks and only 7 phosphopeptides/dephosphopeptides were identified. After enrichment by m-Nb_2O_5–Fe_2O_3, 22 peaks assigned to phosphopeptides/dephosphopeptides were identified with higher intensities and all the high-intensity peaks of non-phosphopeptides were no longer detected, indicating the high enrichment efficiency of m-Nb_2O_5–Fe_2O_3 for phosphopeptides. The detailed information about the phosphopeptides in non-fat milk is summarized in Table S5.

Saliva is an ideal sample in clinic for its non-invasive collection, low cost and carrying lots of information related to disease diagnosis and prognosis [52]. Endogenous phosphopeptides in a saliva sample were enriched with m-Nb_2O_5–Fe_2O_3. MALDI-TOF MS spectra are shown in Fig. S12. Direct analysis identified only 2 phosphopeptides from the MS spectrum which is dominated by non-phosphopeptides. After enrichment, 35 peaks assigned to phosphopeptides were identified with few low-intensity peaks of non-phosphopeptides. Detailed information about the phosphopeptides enriched from human saliva is summarized in Table S6. These results confirmed the pleasing applicability of m-Nb_2O_5–Fe_2O_3 for phosphopeptide enrichment.

To further verify the universal adaptability of the MSPE method, a kind of TCMIs, Reduning injection (RDNI) was employed as an additional real sample. TCMIs, composed of active substances from traditional Chinese medicines, have been widely used in research and clinical practice [53–55]. However, their adverse drug reactions (ADRs) such as acute allergic reactions, might happen in medication. Nevertheless, due to their complex components from natural materials including plants, animal products and minerals, the complete mechanism of how most TCMIs work or react with animal/human bodies remains unclear [56–58]. Among all the possible factors that cause ADRs, protein remnants from plants and animals could be dangerous if injected to animal/human body. Therefore, it is necessary to develop a reliable method for the analysis of proteins including phosphoproteins in TCMIs. To evaluate the effects of the RDNI on digestion and enrichment processes, a mixture of α-casein and β-casein of 0.1 μmol L^{-1} each was spiked into a mixture of different volume ratios of RDNI to water followed by ultrafiltration and tryptic digestion. As shown in Fig. 6A, without enrichment, the spectrum of the blank control with no RDNI added (0:1) was dominated by non-phosphopeptide peaks and only 5 peaks assigned to phosphopeptides were identified. When RDNI was mixed into the solution, all peaks, whether of phosphopeptides or non-phosphopeptides were suppressed heavily by the complex components in the injection, even after the pretreatment before digestion. No phosphopeptides were observed in the mixed solution of a RDNI to water ratio of 1:1 or higher. After enrichment by m-Nb_2O_5–Fe_2O_3, six MS spectra were all dominated by phosphopeptide peaks. Notably, with the increasing proportion of RDNI in the mixed solution, the relative intensities of multi-phosphopeptide peaks increased (m/z 3122), whereas those of mono-phosphopeptide peaks decreased (m/z 1952 and 2556) in the MS spectra. This trend is probably because the complex components in RDNI interfere with the binding between phosphate groups and m-Nb_2O_5–Fe_2O_3 to some extent, and thus m-Nb_2O_5–Fe_2O_3 has a stronger affinity with the peptides containing more phosphate groups in RDNI. When undiluted RDNI was investigated (ratio of 1:0), however, 18 peaks

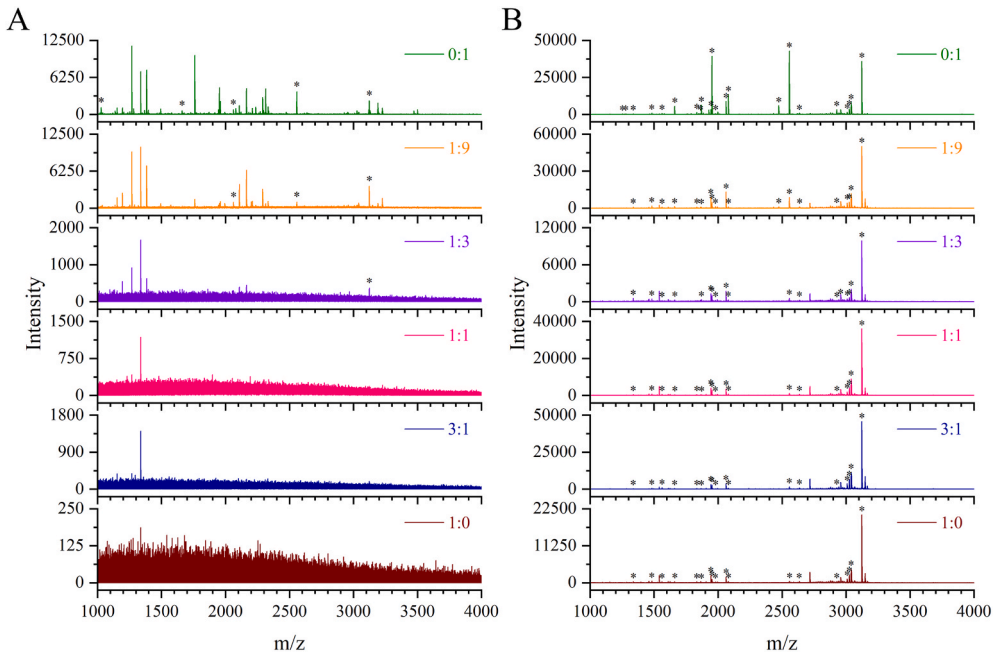

Fig. 6. MALDI-TOF MS spectra of *α*-/*β*-casein-spiked RDNI digests of different ratios of RDNI to water (from 0:1 to 1:0, top to bottom) before (A) and after (B) enrichment with m-Nb_2O_5–Fe_2O_3.

of phosphopeptides/dephosphopeptides were identified, reflecting that the change of intensities affected little on the number of identified phosphopeptides and the satisfactory universality of m-Nb_2O_5–Fe_2O_3. The detailed information about the enriched phosphopeptides from RDNI is summarized in Table S7. Subsequently, the detection limit of phosphopeptides was further determined in RDNI. Undiluted RDNI was spiked with different concentrations of *α*-casein and *β*-casein. As shown in Fig. S13, without enrichment (Fig. S13A), no identifiable peaks were observed in the MS spectra, whether spiked or not. After enrichment, still no peaks were identified in the spectrum (Fig. S13B, control), indicating no presence of high-abundance of phosphoproteins in RDNI. At a spike level of 10 nmol L^{-1}, 8 peaks associated to phosphopeptides were identified in RDNI. With the decrease of the concentration of *α*-/*β*-casein, the identified peaks assigned to phosphopeptides/dephosphopeptides also decreased. However, at a low spike level of 0.5 nmol L^{-1}, still one peak of phosphopeptides was identified in the enriched RDNI, suggesting the low detection limit and high sensitivity of the enrichment of phosphopeptides from RDNI with m-Nb_2O_5–Fe_2O_3.

3.4. Comparison with other reported Nb-based affinity materials

The comparison of m-Nb_2O_5–Fe_2O_3 and other previously reported Nb-based affinity materials in terms of separation mode, anti-interference ability, sensitivity, recovery and applicability is summarized in Table S8. Relative to these existing materials, m-Nb_2O_5–Fe_2O_3 in this work exhibits competitive performance on the listed aspects owing to the unique sandwich-like structure and shows potential for broader applications.

4. Conclusion

This is the first attempt to apply Nb_2C MXene based material in phosphopeptide enrichment. The sandwich-like m-Nb_2O_5–Fe_2O_3 was designed and synthesized by calcining sandwich-like Nb_2C–Fe_3O_4 composites in air without breaking the original MXene feature. The sandwich-like structure based on the layered arrangement of MXene endows the nanocomposite with large specific area and strong magnetism. The most important aspect of this study is the calcination in air provides abundant binding sites of Nb–O and Fe–O on the surface towards phosphopeptides through MOAC mechanism without destroying the sandwich-like structure or eliminating the magnetism. By facile MSPE operation, m-Nb_2O_5–Fe_2O_3 can enrich phosphopeptides with excellent selectivity, strong anti-interference ability and high sensitivity thanks to the synergistic MOAC mechanism provided by Nb_2O_5 and γ-Fe_2O_3 on the surface of m-Nb_2O_5–Fe_2O_3. Moreover, the application of m-Nb_2O_5–Fe_2O_3 in real-world biological and pharmaceutical samples including non-fat milk, human saliva and TCMIs further confirmed the reliability and universality of m-Nb_2O_5–Fe_2O_3 as a promising affinity material for phosphoproteomics.

CRediT authorship contribution statement

Sen Zhang: Data curation, Formal analysis, Investigation, Methodology, Visualization, Writing – original draft. **Yan Lu:** Data curation, Formal analysis, Investigation, Visualization. **Jun-qin Qiao:** Data curation, Formal analysis, Visualization. **Hong-zhen Lian:** Conceptualization, Funding acquisition, Project administration, Resources, Supervision, Writing – review & editing.

Declaration of competing interest

The authors declare that they have no known competing financial interests or personal relationships that could have appeared to influence the work reported in this paper.

Acknowledgements

This work was supported by the National Key Research and Development Program of China (No. 2024YFF0618100) and the National Natural Science Foundation of China (No. 21874065, 22176085 and 22304075).

Appendix A. Supplementary data

Supplementary data to this article can be found online at https://doi.org/10.1016/j.aca.2026.345971.

Data availability

Data will be made available on request.

References

[1] B. Budnik, J. Straubhaar, J. Neveu, D. Shvartsman, In-depth analysis of proteomic and genomic fluctuations during the time course of human embryonic stem cells directed differentiation into beta cells, Proteomics 22 (2022) 2100265.

[2] G.Y. Qing, Q. Lu, Y.T. Xiong, L. Zhang, H.X. Wang, X.L. Li, X.M. Liang, T.L. Sun, New opportunities and challenges of smart polymers in post-translational modification proteomics, Adv. Mater. 29 (2017) 1604670.

[3] A.M. Bode, Z. Dong, Post-translational modification of p53 in tumorigenesis, Nat. Rev. Cancer 4 (2004) 793–805.

[4] G. Simic, M.B. Leko, S. Wray, C. Harrington, I. Delalle, N. Jovanov-Milosevic, D. Bazadona, L. Buée, R. de Silva, G. Di Giovanni, C. Wischik, P.R. Hof, Tau protein hyperphosphorylation and aggregation in Alzheimer's disease and other tauopathies, and possible neuroprotective strategies, Biomolecules 6 (2016) 6.

[5] N. Yin, P.J. Li, X.R. Li, X. Li, Y.M. Wang, X.H. Yu, Y.Y. Deng, C.D. Wang, S. Yu, Increased α-synuclein phosphorylation and oligomerization and altered enzymes in plasma of patients with Parkinson's disease, Neuroscience 567 (2025) 28–36.

[6] B. Domon, R. Aebersold, Review – mass spectrometry and protein analysis, Science 312 (2006) 212–217.

[7] X.S. Li, B.F. Yuan, Y.Q. Feng, Recent advances in phosphopeptide enrichment: strategies and techniques, TrAC-Trends Anal. Chem. 78 (2016) 70–83.

[8] P.J. Boersema, S. Mohammed, A.J.R. Heck, Phosphopeptide fragmentation and analysis by mass spectrometry, J. Mass Spectrom. 44 (2009) 861–878.

[9] B. Eyrich, A. Sickmann, R.P. Zahedi, Catch me if you can: mass spectrometry-based phosphoproteomics and quantification strategies, Proteomics 11 (2011) 554–570.

[10] G.H. Han, M.L. Ye, H.J. Zhou, X.N. Jiang, S. Feng, X.G. Jiang, R.J. Tian, D.F. Wan, H.F. Zou, J.R. Gu, Large-scale phosphoproteome analysis of human liver tissue by enrichment and fractionation of phosphopeptides with strong anion exchange chromatography, Proteomics 8 (2008) 1346–1361.

[11] A.J. Alpert, O. Hudecz, K. Metchtler, Anion-exchange chromatography of phosphopeptides: weak anion exchange versus strong anion exchange and anion-exchange chromatography versus electrostatic repulsion-hydrophilic interaction chromatography, Anal. Chem. 87 (2015) 4704–4711.

[12] M.C. Wang, Y.H. Lee, P.C. Liao, Optimization of titanium dioxide and immunoaffinity-based enrichment procedures for tyrosine phosphopeptide using matrix-assisted laser desorption/ionization time-of-flight mass spectrometry, Anal. Bioanal. Chem. 407 (2015) 1343–1356.

[13] R.Z. Tang, Q. Bai, S.J. Ma, J.J. Ou, Materials, workflows and applications of IMAC for phosphoproteome profiling in the recent decade: a review, TrAC-Trends Anal. Chem. 158 (2023) 116862.

[14] W. Qiu, C.A. Evans, A. Landels, T.K. Pham, P.C. Wright, Phosphopeptide enrichment for phosphoproteomic analysis – a tutorial and review of novel materials, Anal. Chim. Acta 1129 (2020) 158–180.

[15] Y.J. Tan, D.X. Sui, W.H. Wang, M.H. Kuo, G.E. Reid, M.L. Bruening, Phosphopeptide enrichment with TiO_2-modified membranes and investigation of Tau protein phosphorylation, Anal. Chem. 85 (2013) 5699–5706.

[16] Y.Y. Hong, H. Zhao, C.L. Pu, Q.L. Zhan, Q.Y. Sheng, M.B. Lan, Hydrophilic phytic acid-coated magnetic graphene for titanium (IV) immobilization as a novel hydrophilic interaction liquid chromatography–immobilized metal affinity chromatography platform for glyco- and phosphopeptide enrichment with controllable selectivity, Anal. Chem. 90 (2018) 11008–11015.

[17] C.A. Nelson, J.R. Szczech, C.J. Dooley, Q.G. Xu, M.J. Lawrence, H.Y. Zhu, S. Jin, Y. Ge, Effective enrichment and mass spectrometry analysis of phosphopeptides using mesoporous metal oxide nanomaterials, Anal. Chem. 82 (2010) 7193–7201.

[18] C. Wu, S. Zhang, C.Y. Hou, S. Byers, J.F. Ma, In-depth endogenous phosphopeptidomics of serum with zirconium (IV)-grafted mesoporous silica enrichment, Anal. Chem. 96 (2024) 8254–8262.

[19] Y. Huang, Q.H. Shi, C.K. Tsung, H.P. Gunawardena, L. Xie, Y.B. Yu, H.J. Liang, P. Y. Yang, G.D. Stucky, X.A. Chen, An optimized magnetite microparticle-based phosphopeptide enrichment strategy for identifying multiple phosphorylation sites in an immunoprecipitated protein, Anal. Biochem. 408 (2010) 19–31.

[20] X.Z. Wei, X. Wen, H.J. Zheng, Y. Zhang, Q. Jia, Facile synthesis of Fe^{3+} immobilized magnetic polydopamine-polyethyleneimine composites for phosphopeptide enrichment, J. Chromatogr. A 1719 (2024) 464752.

[21] S.B. Ficarro, J.R. Parikh, N.C. Blank, J.A. Marto, Niobium(V) oxide (Nb_2O_5): application to phosphoproteomics, Anal. Chem. 80 (2008) 4606–4613.

[22] H.Y. Lin, W.Y. Chen, Y.C. Chen, Iron oxide/niobium oxide core-shell magnetic nanoparticle-based phosphopeptide enrichment from biological samples for MALDI MS analysis, J. Biomed. Nanotechnol. 5 (2009) 215–223.

[23] X.N. Sun, X.D. Liu, J.A. Feng, Y. Li, C.H. Deng, G.L. Duan, Hydrophilic Nb^{5+}-immobilized magnetic core-shell microsphere – a novel immobilized metal ion affinity chromatography material for highly selective enrichment of phosphopeptides, Anal. Chim. Acta 880 (2015) 67–76.

[24] J.B. Jiang, X.N. Sun, Y. Li, C.H. Deng, G.L. Duan, Facile synthesis of Fe_3O_4@PDA core-shell microspheres functionalized with various metal ions: a systematic comparison of commonly-used metal ions for IMAC enrichment, Talanta 178 (2018) 600–607.

[25] J.B. Jiang, X.N. Sun, X.J. She, J.J. Li, Y. Li, C.H. Deng, G.L. Duan, Magnetic microspheres modified with Ti(IV) and Nb(V) for enrichment of phosphopeptides, Microchim. Acta 185 (2018) 309.

[26] B. Liu, B.C. Wang, Y.H. Yan, K.Q. Tang, C.F. Ding, Efficient separation of phosphopeptides employing a Ti/Nb-functionalized core-shell structure solid-phase extraction nanosphere, Microchim. Acta 188 (2021) 32.

[27] X.Y. Zhang, Q.S. Feng, Z.H. Xie, F.X. Xu, Y.H. Yan, C.F. Ding, A Ti/Nb-functionalized COF material based on IMAC strategy for efficient separation of phosphopeptides and phosphorylated exosomes, Anal. Bioanal. Chem. 414 (2022) 7885–7895.

[28] M. Naguib, V.N. Mochalin, M.W. Barsoum, Y. Gogotsi, 25th anniversary article: mxenes: a new family of two-dimensional materials, Adv. Mater. 26 (2014) 992–1005.

[29] T.T. Mao, F. Zhou, K. Han, Y. Xie, J. Wang, L.C. Wang, Self-standing reduced graphene oxide/Nb_2C MXene paper electrode with three-dimensional open structure for high-rate potassium ion storage, J. Phys. Chem. Solid. 169 (2022) 110838.

[30] P. Wu, X.L. Zhao, Y.X. Ding, Y.F. Huang, D.H. Lin, L.L. Xie, Z.H. Li, Z.G. Zhu, H. L. Zhao, M.B. Lan, Self-assembled multilayer Nb_2C MXene/$MnFe_2O_4$ electrochemical sensor with Schottky junctions for the detection of acetaminophen and dopamine, Colloids Surf. 667 (2023) 131377.

[31] T. Liu, G.Q. Tan, S.J. Feng, B.X. Zhang, Y. Liu, Z.Q. Wang, Y. Bi, Q. Yang, A. Xia, W. L. Liu, H.J. Ren, L. Lv, Dual localized surface plasmon resonance effect enhances Nb_2AlC/Nb_2C MXene thermally coupled photocatalytic reduction of CO_2 hydrogenation activity, J. Colloid Interface Sci. 652 (2023) 599–611.

[32] A.Y. Lu, D. Jiang, L.Y. Pan, X.J. Du, X.L. Shan, W.C. Wang, H. Shiigi, W. Zhang, Z. D. Chen, Defect and interface engineered hierarchical g-C_3N_4 nanotube/Nb_2C MXene schottky heterojunctions: synergistic electrochemiluminescence enhancement and passivation mitigation for high-performance sensing, Chem. Eng. J. 523 (2025) 168386.

[33] X.W. Li, N. Zhang, R.Z. Tang, J.W. Lyu, Z. Liu, S.J. Ma, J.J. Ou, M.L. Ye, Comparative evaluation of MAX-Ti_3AlC_2 and MXene-Ti_3C_2 as affinity chromatographic materials for highly selective enrichment of phosphopeptides, Nanoscale 13 (2021) 2923–2930.

[34] L.Z. Yu, B. Luo, X.X. Zhou, Y.C. Liu, F. Lan, Y. Wu, In situ controllable fabrication of two-dimensional magnetic Fe_3O_4/TiO_2@$Ti_3C_2T_x$ composites for highly efficient phosphopeptides enrichment, ACS Appl. Mater. Interfaces 13 (2021) 54665–54676.

[35] L.Z. Yu, J. He, S. Yan, Y.C. Liu, F. Lan, Y. Wu, Magnetic MXene/PAMAM composites with flexible dimensional regulation for highly effective enrichment of phosphopeptides, ACS Sustainable Chem. Eng. 10 (2022) 2494–2508.

[36] J. He, L.Z. Yu, B. Luo, Y.C. Liu, F. Lan, Y. Wu, Dielectric barrier discharge induced Oxid-$Ti_3C_2T_x$/UiO-66–NH_2 composites for efficient phosphopeptides enrichment, Mater. Des. 233 (2023) 112193.

[37] Y.C. Liu, B. Luo, Z.Y. Li, S.X. Shui, L.Z. Yu, Y. Wu, Metal-phenolic networks modified two-dimensional magnetic MXene-based composites for highly efficient enrichment of phosphopeptides, Microchem. J. 193 (2023) 109114.

[38] F.F. Xu, D.Y. Shang, C.C. Zhu, G.Z. Du, J.S. Shi, X.F. Dong, X.L. Li, X.M. Liang, In situ MXene controlled synthesis of polycrystalline TiO_2 for highly efficient enrichment of phosphopeptides, ACS Appl. Mater. Interfaces 17 (2025) 260–268.

[39] Z.Y. Xia, Y.W. Lin, J.H. Sun, Y. Wang, X.F. Hu, C.H. Deng, Magnetic MXene with dual Ti-affinity sites for enhanced phosphopeptide enrichment in saliva, Microchim. Acta 192 (2025) 840.

[40] S. Zhang, J.-Y. Li, W. Gao, J.-Q. Qiao, H.-Z. Lian, Magnetic Ti_3C_2 MXene nanosheets prepared for enrichment of phosphopeptides, ACS Appl. Mater. Interfaces 15 (2023) 16505–16514.

[41] S. Zhang, X.D. Yang, F. Zhang, J.Q. Qiao, W.J. Zheng, H.Z. Lian, Potato-chip-like two-dimensional magnetic trimetallic oxides derived from MXene-MOF nanocomposites for fast enrichment of phosphopeptides, Sep. Purifi. Technol. 382 (2026) 135918.

[42] Y.L. Bai, X.D. He, R.G. Wang, Lattice dynamics of Al-containing MAX-phase carbides: a first-principle study, J. Raman Spectrosc. 46 (2015) 784–794.

[43] M.A.S. Sakr, H. Abdelsalam, N.H. Teleb, M.A. Saad, O.H. Adb-Elkader, Y.S. Liu, Q. F. Zhang, Exploring the drug delivery capabilities of Nb_2C MXene functionalized with oxygen and fluorine: a DFT study, J. Mol. Graphics Modell. 136 (2025) 108937.

[44] O.M. Lemine, N. Madkhali, M. Alshammari, S. Algessair, A. Gismelseed, L. El Mir, M. Hjiri, A.A. Yousif, K. El-Boubbou, Maghemite (γ-Fe_2O_3) and γ-Fe_2O_3–TiO_2 nanoparticles formagnetic hyperthermia applications: synthesis, characterization and heating efficiency, Mater 14 (2021) 5691.

[45] H. Lin, S.S. Gao, C. Dai, Y. Chen, J.L. Shi, A two-dimensional biodegradable niobium carbide (MXene) for photothermal tumor eradication in NIR-I and NIR-II biowindows, J. Am. Chem. Soc. 139 (2017) 16235–16247.

[46] O.N. Shebanova, P. Lazor, Raman spectroscopic study of magnetite ($FeFe_2O_4$): a new assignment for the vibrational spectrum, J. Solid State Chem. 174 (2003) 424–430.

[47] S.E. More, S.A. Raut, S. Prekumar, S.R. Bhopale, D. Deduytsche, S.V. Bhoraskar, M. A. More, D. Thiry, C. Detavernier, N. De Geyter, V.L. Mathe, R. Morent, Oxidation behavior of iron and binder-mixed iron: insights from TGA–DSC and in situ XRD analysis for field emission application, Mater. Adv. 7 (2026) 198.

[48] J.F. Xi, X.J. Liu, L. Zhang, Z.W. Zhang, J.C. Zhuo, T. Du, Y.J. Zhang, J.Y. Duan, H. L. Dong, J.L. Wang, Engineering of schotty heterojunction in Ru@Bi_2S_3/Nb_2C MXene based on work function with enhanced carrier separation for promoted sterilization, Chem. Eng. J. 473 (2023) 145169.

[49] Q.Q. Feng, Z.F. Chen, K. Zhou, M.L. Sun, X.R. Ji, H. Zheng, Y. Zhang, Hydrothermal synthesis of γ-Fe_2O_3/rGO hybrid nanocomposite as an efficient electrocatalyst for the oxygen reduction reaction, ChemistrySelect 6 (2021) 8177–8181.

[50] F.Y. Kong, X.D. He, Q.Q. Liu, X.X. Qi, D.D. Sun, Y.T. Zheng, R.G. Wang, Y.L. Bai, Further surface modification by carbon coating for in-situ growth of Fe_3O_4

nanoparticles on MXene Ti_3C_2 multilayers for advanced Li-ion storage, Electrochim. Acta 289 (2018) 228–237.
[51] L.B. Wang, H. Liu, X.L. Lv, G.Z. Cui, G.X. Gu, Facile synthesis 3D porous MXene $Ti_3C_2T_x$@RGO composite aerogel with excellent dielectric loss and electromagnetic wave absorption, J. Alloys Compd. 828 (2020) 154251.
[52] L.M. Sreebny, Saliva in health and disease: appraisal and update, Int. Dent. J. 50 (2000) 140–161.
[53] X.R. Lou, H. Chen, N. Shi, R.X. Yu, S.L. Li, Y. Yang, S.Q. Liu, J.F. Xie, H.B. Qiu, Treatment effects of Xuebiqing injection in patients with sepsis by clinical phenotype: a post hoc analysis of the EXIT-SEP trial, eClinicalMedicine 86 (2025) 103341.
[54] X.Y. Zhang, X.Y. Lao, S.C. Liao, C.Y. Ye, C. Wang, Efficacy of Shenkang injection combined with renin-angiotensin-aldosterone system blockers in diabetic nephropathy: a systematic review and meta-analysis of randomized controlled trials, Ren. Fail. 47 (2025) 2499231.
[55] S.C. Li, Y.Q. Wang, X.Y. Sun, L.Y. Lu, Y. Yong, X.N. Kong, J.A. Song, Suppressing neuroinflammation by Shenfu injection against ischemic stroke in mice via inhibiting RAGE-PI3K-Akt pathway, Phytomedicine 144 (2025) 156940.
[56] W. Zhuang, G. Sun, X.L. Lin, B. Chen, L. Wu, D.C. Jiang, S.Y. Xi, Medication with caution: analysis of adverse reactions caused by a combination of Chinese medicine and warfarin sodium tablets, J. Ethnopharmacol. 254 (2020) 112586.
[57] X.B. Zhu, M. Guo, Z.H. Zhang, L.H. Sun, L. Liu, L.J. Zhou, C.L. Shan, Y. Yang, L. D. Kan, L.C. Li, Chinese herbal injections for coronavirus disease 2019 (COVID-19): a narrative review, Integr. Med. Res. 10 (2021) 100778.
[58] R. Zheng, L.Y. Tao, J.S.W. Kwong, C.M. Zhong, C.Y. Li, S.Q. Chen, Y. Sun, X. Y. Zhang, H.C. Shang, Risk factors associated with the severity of adverse drug reactions by Xiyanping injection: a propensity score-matched analysis, J. Ethnopharmacol. 250 (2020) 112424.